Application of a semianalytical strain assessment and multiaxial fatigue analysis to compare rolling contact fatigue in twin-disk and full-scale

Citation for the original published paper (version of record):

N.B. When citing this work, cite the original published paper.

(article starts on next page)

ORIGINAL ARTICLE

FFEMS Fatigue & Fracture of Engineering Materials & Structures WILEY

Application of a semianalytical strain assessment and multiaxial fatigue analysis to compare rolling contact fatigue in twin-disk and full-scale wheel/rail contact conditions

Nicola Zani[1] | Magnus Ekh[2] | Anders Ekberg[3] | Angelo Mazzù[1]

[1]Department of Mechanical and Industrial Engineering, University of Brescia, Brescia, Italy

[2]Department of Industrial and Materials Science/CHARMEC, Chalmers University of Technology, Gothenburg, Sweden

[3]Department of Mechanics and Maritime Sciences/CHARMEC, Chalmers University of Technology, Gothenburg, Sweden

Correspondence
Nicola Zani, Department of Mechanical and Industrial Engineering, University of Brescia, Via Branze, 38, 25123 Brescia, Italy.
Email: nicola.zani@unibs.it

Abstract

A semianalytical model is introduced to assess rolling contact fatigue problems in railway applications. The constitutive law is based on the nonlinear kinematic and isotropic hardening model of Chaboche–Lemaitre, which allows the cyclic elastoplastic strain under the contact surface to be evaluated. The much higher computational effectiveness in comparison with finite element (FE) analyses is quantified. The Dang Van multiaxial fatigue criterion is implemented to evaluate the rolling contact fatigue in the subsurface elastic region where cracking is relatively rare but more dangerous than surface cracks. The influence of the presence of sulfides in the wheel matrix in decreasing fatigue strength is also assessed by means of Murakami's approach. The model is used to compare conditions under small-scale twin-disk experiments to full-scale wheel/rail contact conditions. It is found that, for the same Hertzian pressure, the small-scale contact is more conservative in that it causes a deeper plasticized layer as compared with the elliptical full-scale contact. In the investigated cases, crack initiation is also not expected according to Dang Van criterion in neither of the studied contact conditions.

KEYWORDS

fatigue limit, finite element models (FEM), multiaxial fatigue, ratcheting, semianalytical model (SAM), shakedown

1 | INTRODUCTION

The trend towards heavier axle loads for freight transport and higher speed passenger trains has increased demands on the design of railway components (e.g., wheels and rails). Rolling contact fatigue (RCF), together with wear and tread damage, are common reasons for premature wheel removal, which are a significant cost factor for

railroad and car owners. Suboptimal design of these components may cause economic costs, train delays, unplanned maintenance, personal injuries, and shorten components' operational lives. In addition, proper design may reduce CO_2 emissions and energy consumption.

The railway industry must follow specific requirements to run safely. In this regard, railway component manufacturers may carry out full-scale tests on a

machine typically composed of two disks with rail profiles on which the wheelset is placed. This apparatus enables investigation of the vehicle dynamics and wheel profile wear[1,2]; however, it is of limited use for investigations into wear and RCF resistance of different materials.

Small-scale test machines are also widely used in metallurgical research to investigate the performance of railway steels in terms of wear and RCF. To replicate full-scale rolling contact conditions and vary the slip value, twin-disk testing can be used. In this type of test, two disks made from wheel and rail materials are hydraulically loaded in contact and rolled at varying speeds to achieve a prescribed slip. With small-scale specimens, we can efficiently run experiments with clean and dry contact and in the presence of contaminants, like sand particles,[3–5] leaves,[6,7] and water.[8–11] Furthermore, the material response and damage characteristics under these conditions are very similar to those found in actual wheels, such as the effect of the contaminants on adhesion, resulting plastic deformation, wear, and RCF.

In addition to experimental models, numerical and semianalytical models have been developed to predict material behavior. Semianalytical methods (SAMs) comprise a group of computational methods based on the summation of analytical solutions to describe complex problems. Compared with finite element (FE) analyses, the significant advantages of SAMs are their relative computational speed and robustness in resolutions. Therefore, SAMs have been adopted especially for complex problems that would require long computational times with FE analysis, where solving thousands or even millions of loading cycles would be cumbersome with numerical solvers.[12–17]

Several SAM solvers have been developed to study traditional contact problems (such as the cylindrical line contact problem and the point contact problem).[18–22] In these works, the main task was to investigate the cyclic behavior of the materials. First, the contact pressure was directly solved from the geometric parameters and the elastic properties using the Hertzian theory. The associated stress components were then found using the elastic theory, which enables a quicker solution. Merwin and Johnson[23] and Bhargava et al.[24] employed the elastic stress framework to calculate potential plastic fields. The elastic stresses were then taken as input for the constitutive solvers.

Among the different plasticity models, one commonly used for RCF and cyclic plasticity is the Chaboche–Lemaitre model,[25] which accounts for mixed nonlinear combined hardening. This model applies the superimposed kinematic hardening proposed by Armstrong and Frederick[26] and Voce[27] based on an isotropic hardening model. Simulations featuring the Chaboche–Lemaitre model can capture material responses featuring elastic shakedown, plastic shakedown, or ratcheting, as reported by Donzella et al.[28] and Foletti and Desimone.[18]

Knowing the cyclic response lets us understand the associated damage phenomenon. Ratcheting causes severe plastic deformation of the surface material leading to surface fatigue failures caused by the accumulated plastic strain. These failures are relatively innocuous in that they result in the detachment of small pieces of tread materials. For these cracks, wear will limit the crack growth.[28] Low cycle fatigue is closely associated with plastic deformation of the material. In wheels and rails, it may occur in locations and under load conditions that cause plastic deformation, but less accumulation of plastic strain than what would cause ratchetting failures. Finally, high cycle fatigue relates to an elastic material response potentially following minor plastic deformations following the first load cycles. High cycle fatigue generally occurs at some depth below the contact surface of rails and wheels. Cracks initiating below the contact surface are rare but more dangerous than surface cracks; therefore, the ability to predict this kind of failure is vital. Subsurface crack initiation is promoted by the presence of material defects like nonmetallic inclusions.

Various criteria have been developed to assess multiaxial high cycle fatigue of components subjected to RCF, such as railway wheels and rails. Various authors[29–31] have proposed the use of the Dang Van criterion to predict subsurface-initiated RCF.[32] This choice is often justified on the basis of multiaxial fatigue tests on specimens subjected to loads approximately matching the subsurface stresses.[31]

This paper compares the twin-disk contact problem to the wheel–rail full-scale problem through a SAM analysis. First, a parametric study is carried out with different load levels in which the accumulated plastic shear strain characterizes the material response. This is a suitable approach to in relation to ratchetting failures. Then, the Dang Van multiaxial fatigue model is employed to predict subsurface crack initiation, considering the effect of nonmetallic inclusions in the material.

2 | SEMIANALYTICAL MODEL

The SAM code was developed in MATLAB®. The software can evaluate the Hertzian contact stresses for elliptical and cylindrical bodies. Although the former refers to a three-dimensional geometrical problem, the latter is limited to a plane strain problem. The main geometrical parameters are shown in Figure 1: R_{1x}, R_{2x}, R_{1y}, and R_{2y} are radii of curvature, ω is the angle between the two elliptical bodies, L is the length of the cylindrical contact,
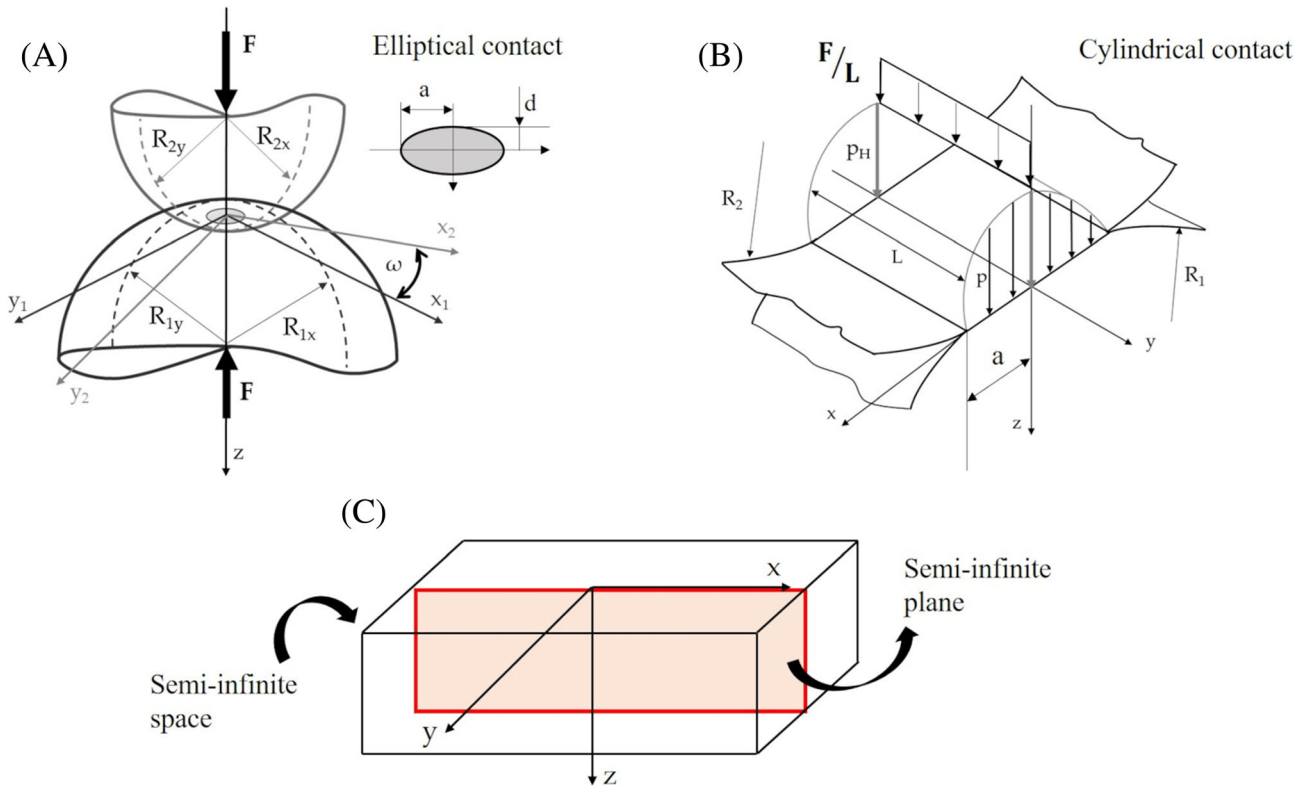
FIGURE 1   Scheme of the model: (A) elliptical contact, (B) cylindrical contact, and (C) semi-infinite plane and space [Colour figure can be viewed at wileyonlinelibrary.com]

and F is the contact force. According to the specific problem, the body in contact was assumed to be either a semi-infinite space or a plane. Figure 1C shows the adopted frame of reference: The xz plane where the stress history is evaluated coincides with the rolling plane.

The first step in the analysis is to calculate the contact area and pressure. This step was performed by applying the Hertzian formulation for line and elliptical contact. Next, the tangential load distribution was obtained by scaling the pressure distribution by the friction coefficient, assuming full-slip conditions.

Next, the computational domain was defined as a parallelepiped with dimensions $x = 3a$, $z = 1.5a$, and (only for the elliptic case) $y = 1.1a$. In this domain, we defined a grid of points (103 along the x direction, 52 in the z direction, and 21 in the y direction). The Cauchy elastic stress due to the normal and tangential loading at a general point (x, z) on the xz plane was calculated through McEwen's and Boussinesq's equations on line and elliptical contact, respectively. Two different criteria were adopted because McEwen's equations can be solved analytically to provide the solution for the whole domain (see Appendix A for equations). In contrast, Boussinesq's problem must be solved numerically, and the singularity points of the equations prevent a solution near the contact surface (see Appendix B for equations).

The stress history on the rolling plane served as the input data to the constitutive analysis. The plastic strain increment was obtained through a cyclic plasticity model[25] with mixed nonlinear isotropic and kinematic hardening. The yield function Φ was assumed to be of von Mises type and defined in terms of the deviatoric stress σ_{dev}, the backstress X, the dragstress R, and the initial yield stress σ_y:

$$\Phi = \sqrt{\frac{3}{2}}\|\sigma_{dev} - X\| - (R + \sigma_y) \leq 0. \qquad (2.1)$$

The evolution of the kinematic hardening was defined by Armstrong and Frederick[26]:

$$\dot{X} = C\dot{\lambda}\frac{\sigma_{dev} - X}{|\sigma_{dev} - X|} - \gamma\dot{\lambda}X. \qquad (2.2)$$

In addition, the nonlinear evolution equation for the isotropic hardening $\dot{R}$ is defined by

$$\dot{R} = \dot{\lambda}b(R_\infty - R), \qquad (2.3)$$

where C is the initial kinematic hardening, γ controls the kinematic saturation hardening, b controls the initial

isotropic hardening, and R_∞ is the isotropic saturation hardening. The evolution equation of the plastic strain is given by

$$\dot{\varepsilon}^p = \dot{\lambda}\sqrt{\frac{3}{2}\frac{\boldsymbol{\sigma}_{dev} - \boldsymbol{X}}{|\boldsymbol{\sigma}_{dev} - \boldsymbol{X}|}}. \qquad (2.4)$$

The variable $\dot{\lambda}$ is a function of the equivalent plastic strain rate $\dot{\varepsilon}^p$:

$$\dot{\lambda} = \sqrt{\frac{2}{3}\dot{\boldsymbol{\varepsilon}}^p : \dot{\boldsymbol{\varepsilon}}^p} \qquad (2.5)$$

Numerical implementation featured backward Euler time integration and the Newton–Raphson procedure to solve the nonlinear system.

Finally, it should be pointed out that the main weak point of this solver based on an analytical solution of the contact pressure is that it cannot consider the residual stress because after the loading cycle, the stress is always zero, which is valid only in the case where the material does not plasticize. Some relaxation procedures dealing with the stress/strain relaxation in line contact are available in literature.[21–23] However, these models were only validated in the first cycles and for specific stress/strain components, and simulations involving hundreds/thousands of cycles were not discussed. Relaxation procedures for elliptical contact are not available, instead.

3 | CASE STUDY

The twin-disk experimental test performed by Mazzù et al.[33] was used as a small-scale reference. There, rolling contact tests were carried out by coupling the ER8 EN13262 wheel steel with UIC 900A rail steel. The wheel and rail samples had diameters of 60 and 59.5 mm, respectively, and the contact width varied from 8 to 10 mm, as shown in Tables 1 and 2. Three different loads F were imposed by varying the theoretical Hertzian pressure predicted by the cylindrical contact theory. The estimated coefficient of friction was roughly 0.68.[33] The twin-disk problem can be addressed with the SAM by solving the plane strain cylindrical contact, setting the two radii of curvature R_{1x} and R_{2x} as the radii of the specimens, the transversal curvatures R_{1y} and R_{2y} as infinite, and the out-of-plane length L as the contact width.

For the full-scale problem, we considered a wheel with a diameter of 900 mm and a rail with a transverse curvature radius of 600 mm. The applied load was estimated to provide the same maximum pressure as in the twin-disk setup (Table 3). The wheel–rail contact was simulated such that the wheel and rail are cylinders with orthogonal axes; therefore, in the SAM, R_{1x} was the wheel radius, and R_{2y} was the rail radius, whereas the other curvatures were considered infinite. This resulted in an elliptical contact problem.

Table 4 shows the elastic–plastic properties of the ER8 EN13262 wheel steel; Young's modulus and Poisson's ratio of the rail were set equal to the wheel values.[9] The isotropic and kinematic hardening parameter values were taken from Donzella et al.[34] Note that in Donzella et al.,[34] the parameter values were identified on the basis of twin-disk test data to account for realistic (multiaxial) stress conditions.

4 | SEMIANALYTICAL VERSUS FE STRESS/STRAIN ANALYSIS

For validation purposes, a comparison with FE analyses was carried out. The maximum contact pressure in Condition 3 described in Tables 1 and 3 was chosen to compare the FE and SAM results. This loading condition was chosen because it resulted in the highest level of plasticity, and therefore, the SAM results are likely to show the largest deviations from the FE analysis. Three loading

TABLE 2 Dimensions of the bodies in contact

| Twin-disk		Wheel–rail	
R_{1x} (mm)	30	R_{1x} (mm)	460
R_{1y} (mm)	Inf	R_{1y} (mm)	Inf
R_{2x} (mm)	29.75	R_{2x} (mm)	Inf
R_{2y} (mm)	Inf	R_{2y} (mm)	300

TABLE 1 Loading conditions for the twin-disk contact

Condition no.	Contact force F (kN)	Theoretical contact pressure (MPa)	Contact semiaxis a (mm)	L (mm)	Friction coefficient f
1	1500	673	0.178	8	0.68
2	2490	777	0.204	10	0.68
3	3830	963	0.253	10	0.68

TABLE 3 Loading conditions for the wheel–rail contact

Condition no.	Contact force F (kN)	Theoretical contact pressure (MPa)	Pressure half-length $a \times d$ (mm × mm)	Friction coefficient f
1	16.5	673	3.91 × 2.98	0.68
2	23.7	777	4.33 × 3.36	0.68
3	45	961	5.37 × 4.46	0.68

TABLE 4 Elastoplastic material parameters

Young's modulus (GPa)	Poisson's ratio	Initial yield stress (MPa)	R_∞	b	C (MPa)	γ
206	0.3	330	210	0.3	400,000	30
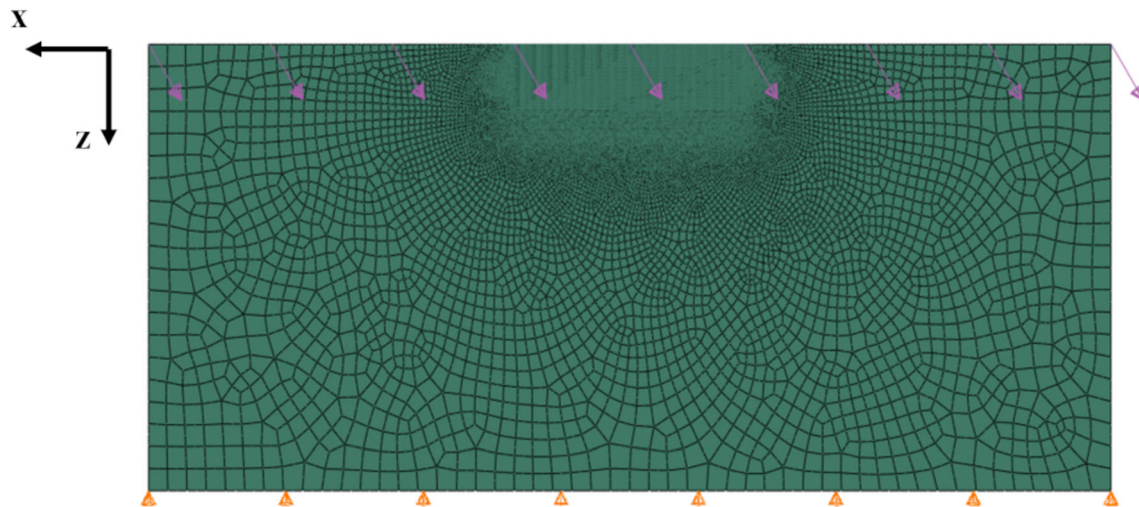
FIGURE 2 FE model for validation of the twin-disk problem (the violet arrows represent the direction of the surface traction force and the orange triangles the boundary constraints) [Colour figure can be viewed at wileyonlinelibrary.com]

cycles were simulated to investigate the effect of cyclic hardening.

FE simulations were performed using the commercial software Abaqus® 2020.[35] The model geometries and FE meshes are shown in Figures 2 and 3. For twin-disk contact, the specimen was approximated as a flat body, and the smallest element size in the surface region was approximately 10 μm. Linear plane strain quadrilateral elements (CPE8R) were used. For the full-scale problem, the semi-infinite space was modeled as a paralepipid meshed with linear hexahedral elements (C3D8R) with the smallest element size of 1 mm in the contact area. In both cases, the geometry was clamped at the lower surface.

The contact load was defined by an UTRACLOAD subroutine that allowed for a specific general pressure load to be applied on the upper surface. The load magnitude was defined from the vector sum of the contact pressure and the frictional load parallel to the surface (which is proportional to the contact pressure):

$$P(x,y) = p(x,y)\sqrt{1+f^2}, \quad (4.1)$$

where $P(x, y)$, $p(x, y)$, and f are the surface traction magnitude, Hertzian pressure, and friction coefficient, respectively (the transversal component y was neglected in the line contact problem).

4.1 | Stress distribution

Normalized stress components (stress divided by maximum Hertzian pressure) were compared. In general, a close agreement in the surface and subsurface stress distribution was observed between twin-disk and wheel–rail conditions. A detailed comparison was made of stresses at the surface—$z/a = 0$ for line contact (twin-disk) and $z/a = 0.1$ for elliptical contact (wheel–rail) to avoid the influence of the singularity points. Results are presented in Figure 4. A similar analysis
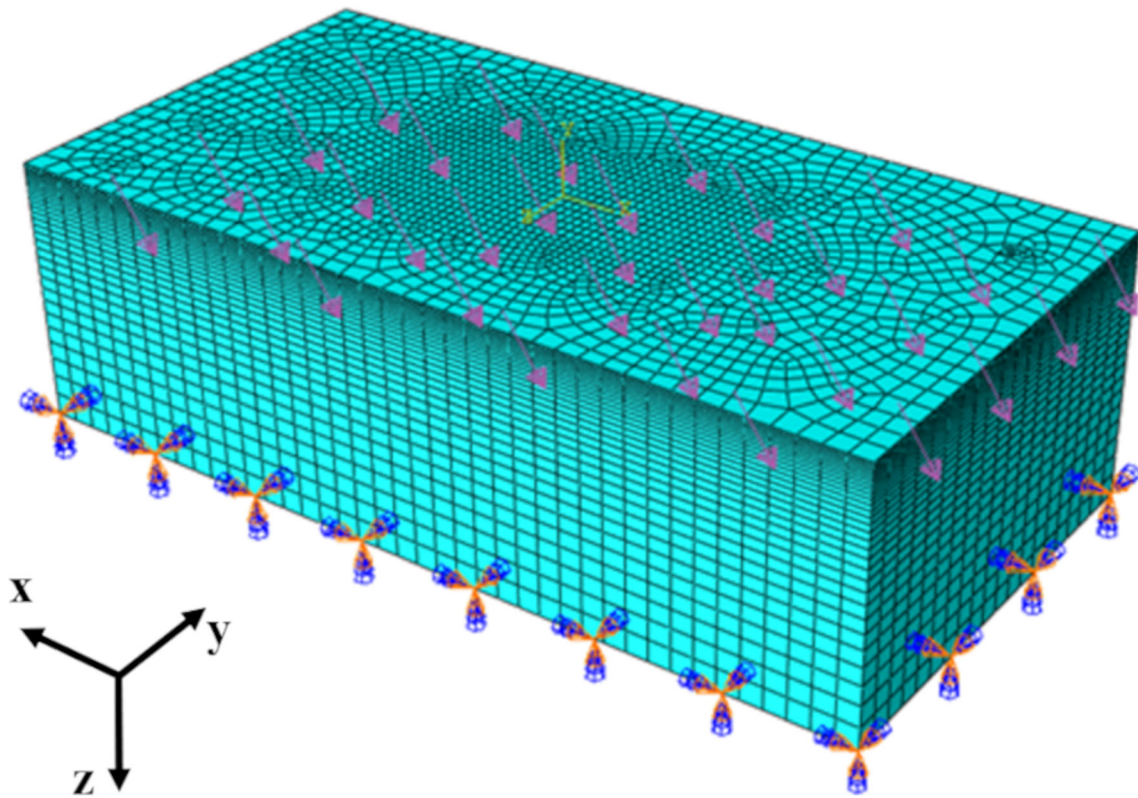
FIGURE 3 FE model for validation for wheel–rail contact (the violet arrows represent the direction of the surface traction force and the orange triangles the boundary constraints) [Colour figure can be viewed at wileyonlinelibrary.com]

made for $z/a = 0.5$ showed less differences between the load cases.

4.2 | Plastic strains

The plastic strain components acting in the rolling xz plane were compared at the end of the last load cycle. To properly account for the effect of the stress and strain relaxation, the FE results were considered at a distance of $2a$ from the center of the contact of the last load step. In Figure 5, strain components are plotted against the dimensionless depth z/a. The SAM results show a qualitative trend similar to the FE results; however, the SAM predicted slightly higher magnitudes of normal plastic strain. This can be ascribed to the lack of a procedure for stress relaxation that can redistribute residual stresses and strains. More specific, the plastic shear strain estimated by the SAM aligns well with FE results in the subsurface region, whereas the surface strain is more conservative. The conclusion is that the coded model can predict the dominating strain component in the rolling contact problem with good accuracy.

Table 5 shows details regarding computing time and model dimensions. As expected, the SAM is much faster than the numerical solver.

5 | RESULTS

5.1 | Plastic deformation

The accumulated plastic shear strain γ_{xz} was chosen for the comparison between the case studies because it is considered as the primary source of the plastic flow in contact.

Figure 6 shows the plastic shear strain evolution at different depths (up to $z/a = 1$). The contact load, defined by the combination of the contact pressure and the traction force, evidently influences the shear strain for instance, from the lowest pressure (673 MPa) to the highest (960 MPa). In Figure 6, it is seen that γ_{xz} dramatically increases by more than a factor 2. Moreover, the strain accumulation rate increases from the subsurface to the surface region.

There were no significant differences between the surface strains ($z/a = 0.05$) estimated in small-scale
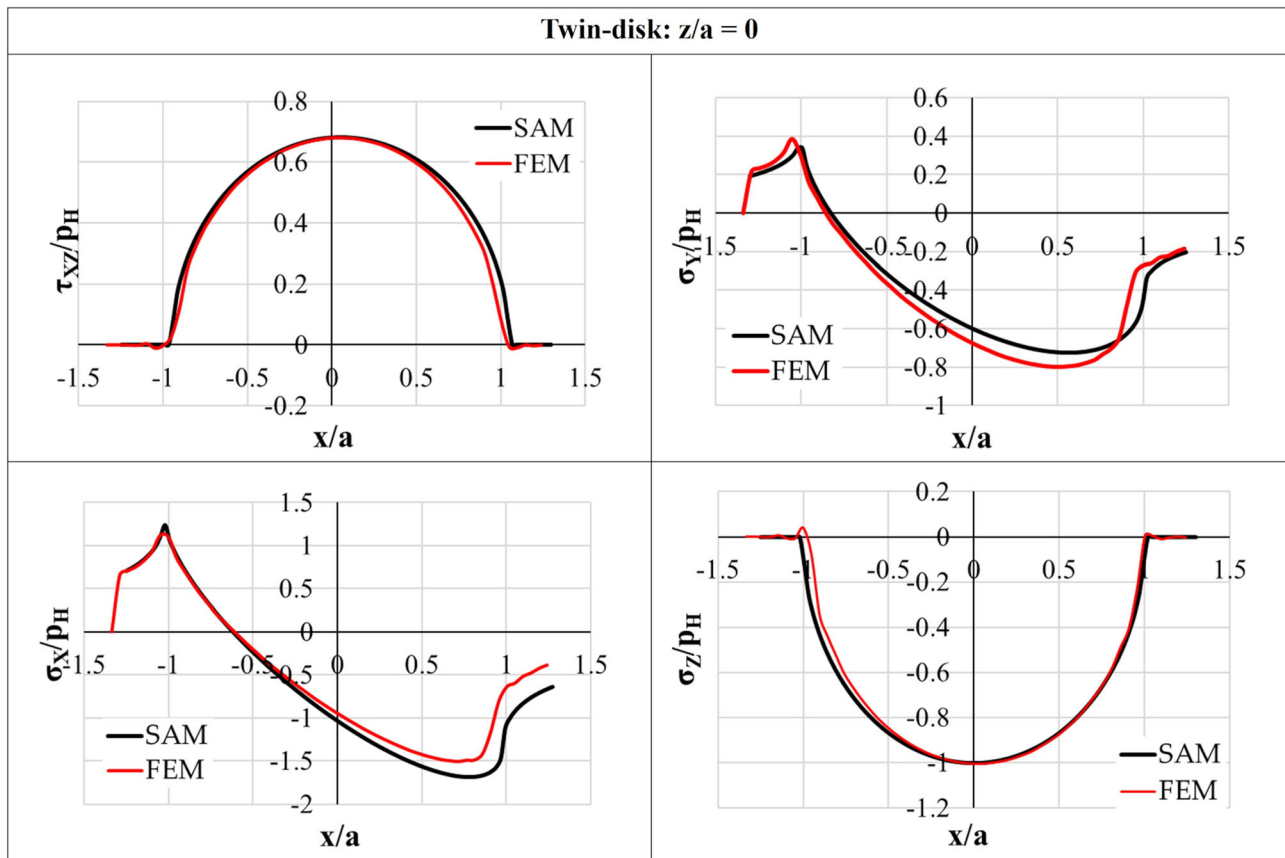
FIGURE 4 Stress component comparisons between SAM and FE analyses for stresses at the surface [Colour figure can be viewed at wileyonlinelibrary.com]

and full-scale conditions. The reason is that the same contact stresses are applied in both cases. By contrast, higher plastic shear strains in the subsurface region are predicted for the twin-disk conditions, as is also reported in Mazzù and Donzella.[20] Figure 7, where γ_{xz} is plotted as a function of depth, better clarifies how the plasticized layer is deeper in line contact. This suggests that the alternating shear stress decreases faster with depth in elliptical contacts. Furthermore, the graphs reveal that not all of the control area undergoes plastic deformation. Though not visible in the figure, three regions can be identified according to their cyclic response: (i) a surface layer with ratcheting, (ii) an intermediate region subjected to elastic shakedown, and (iii) a region that always shows an elastic response. Table 6 indicates that the depths of these regions clearly depend on the applied load and the contact geometry. In general, the twin-disk models did not predict any elastic responses for $z/a < 1.5$, in contrast to the full-scale model. Figure 8 also shows that the threshold separating the ratcheting area from the elastic shakedown area is deeper for line contact compared with elliptical contact, particularly for

contact pressures of 673 and 777 MPa, in which it is double. These results also highlighted that the non-linearity of the constitutive model does not allow to extrapolate the cyclic behavior only from the first load cycles.

Figure 8 shows optical micrographs of the disks tested under Conditions 1 and 2[33]—the white lines represent the plastic flow line at the end of the test, and the red line defines the z/a threshold for the elastic shakedown. The micrographs, illustrating the cross section in the center of the disk, reveal a surface layer with severe plastic flow with the flow lines stretched in the direction of the applied surface friction. Below this area, the strain bands are less marked, and the flow lines become orthogonal to the surface specimen (see Figure 9). However, the comparison can only be made from a qualitative point of view because the proposed model does not consider all the phenomena occurring in the contact area, such as wear. In addition, the twin-disk test is not fully two-dimensional because boundary effects exist and the number of cycles in the experiments was higher than in the simulations.
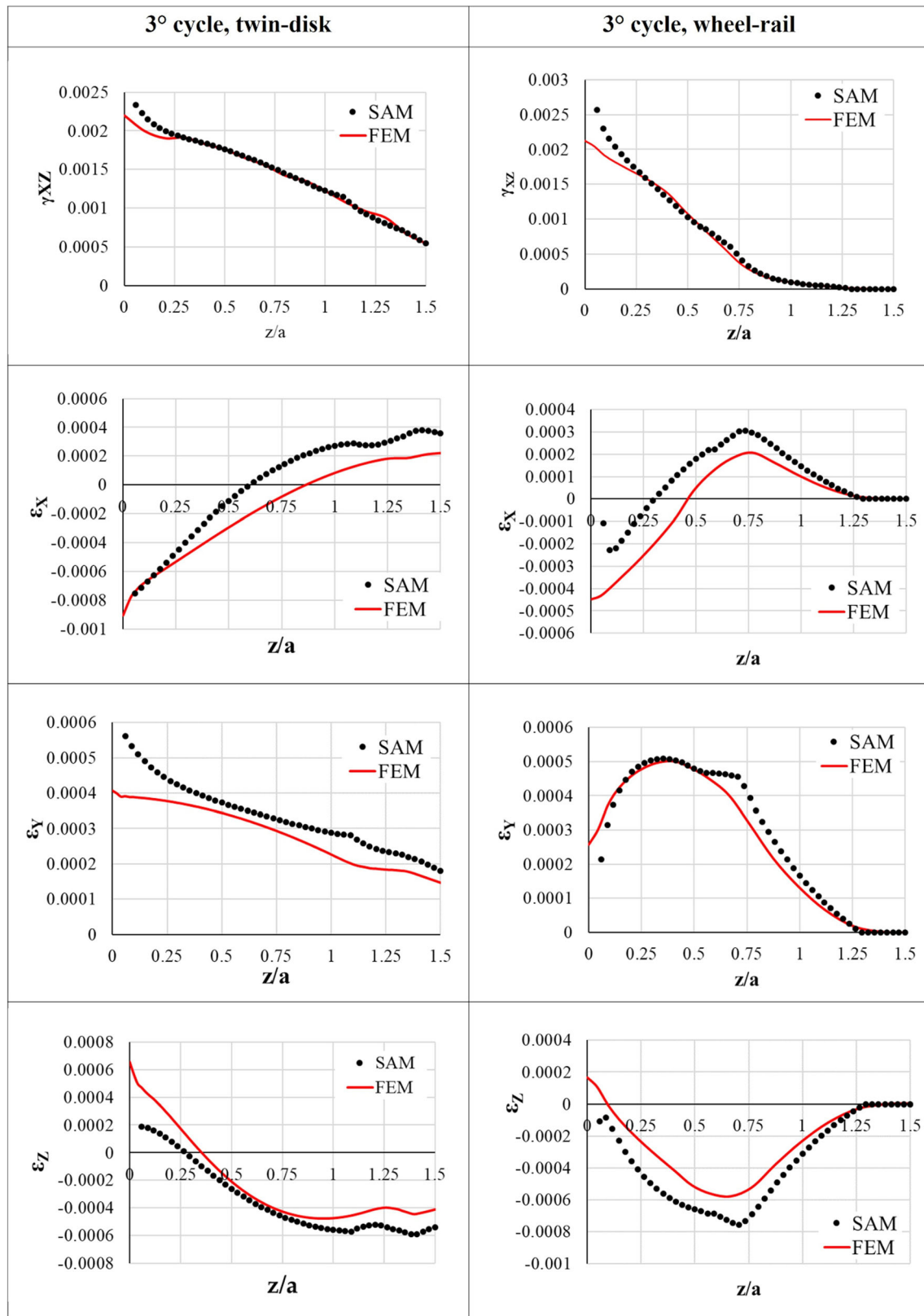
FIGURE 5   Plastic strain comparison between the SAM and the FE analyses [Colour figure can be viewed at wileyonlinelibrary.com]

TABLE 5 Details about the simulations

	Twin-disk		Wheel–rail	
	FEM	SAM	FEM	SAM
Number of cycles	3			
Number of nodes	173,386	5356	67,425	5356
Number of elements	57,645	—	64,230	—
Computing time	0.5 h	~11 s	3 h	~5 min

5.2 | Multiaxial fatigue failure (subsurface cracking)

The cyclic material response obtained with the SAM was used to assess high cycle fatigue using the Dang Van criterion,[30,32] which is commonly used for multiaxial (rolling contact) fatigue. The Dang Van equivalent stress σ_{DV} can be expressed as
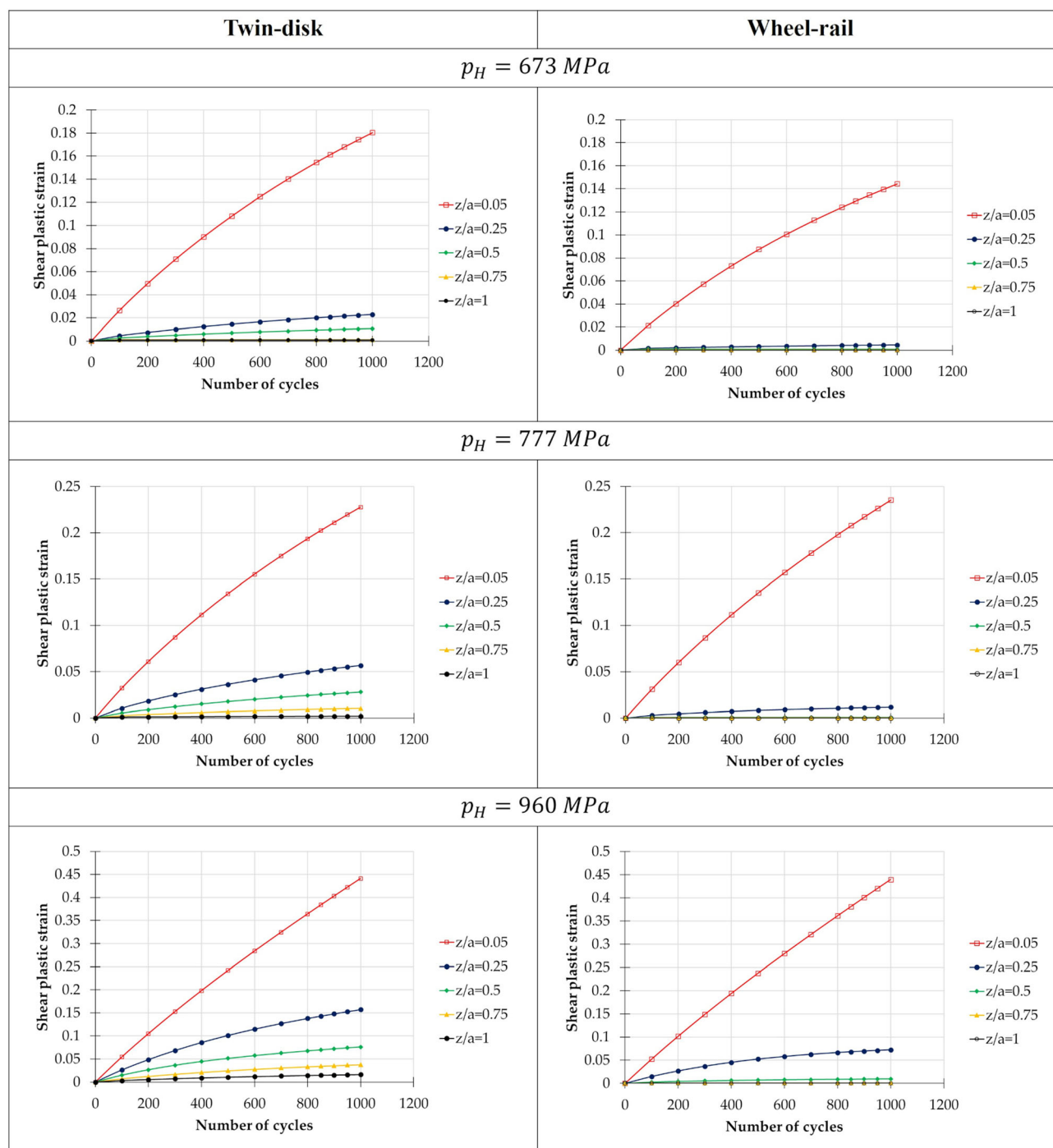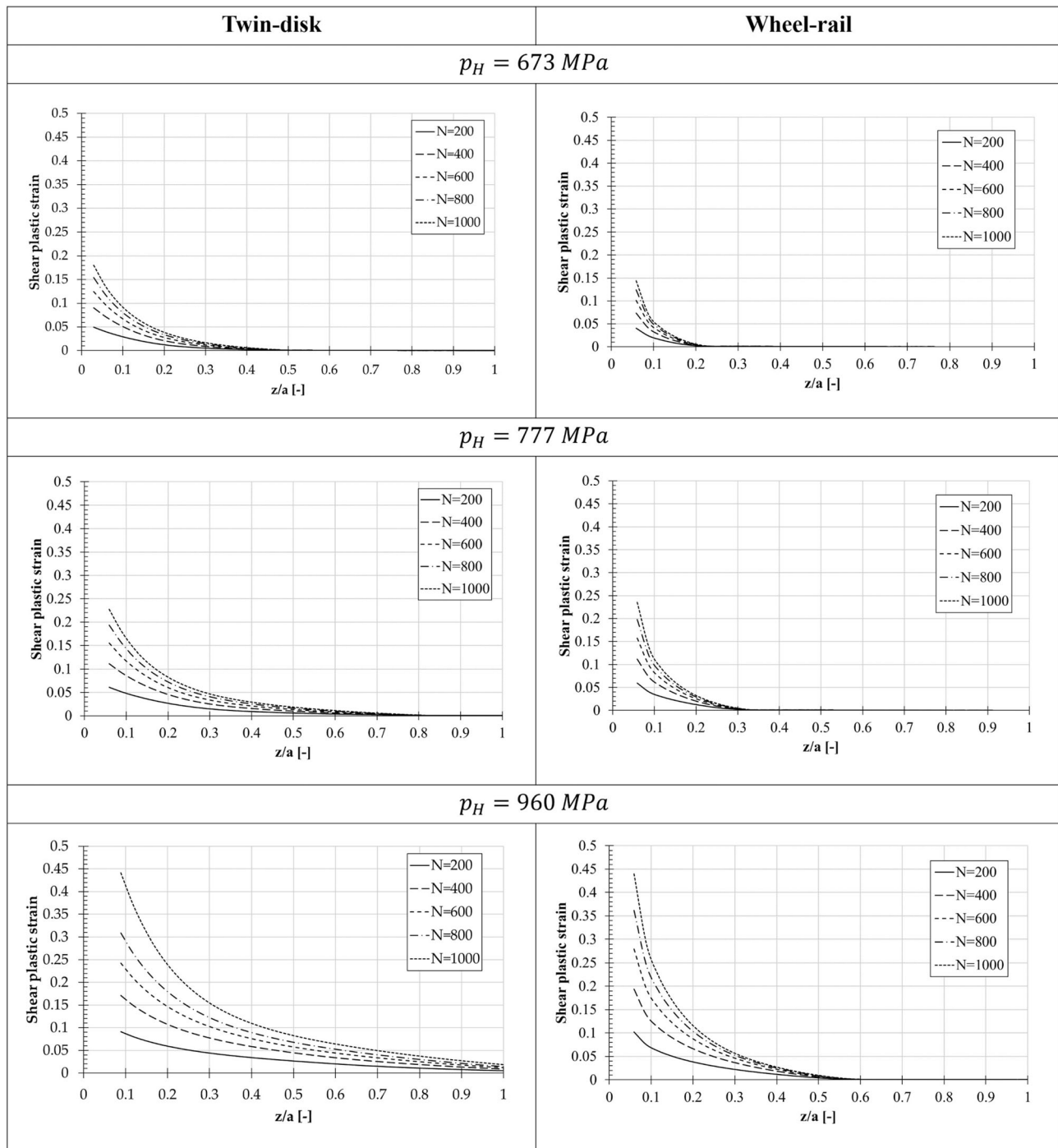

FIGURE 6 Shear plastic strain rate as a function of the number of cycles [Colour figure can be viewed at wileyonlinelibrary.com]

	Twin-disk			Wheel-rail		

FIGURE 7 Shear plastic strain along the dimensionless depth z/a

	Twin-disk			Wheel–rail		
Hertzian pressure (MPa)	673	777	960	673	777	960
z/a for elastic shakedown	0.5	0.73	0.94	0.24	0.35	0.62
z/a for elastic response	—	—	—	0.94	1	1.26

TABLE 6 Dimensionless depths z/a identifying areas subjected to elastic shakedown and fully elastic response

FIGURE 8 Microstructure under the contact surface of the steel wheel disk tested with $p_H = 673$ MPa (A) and $p_H = 777$ MPa (B).[33] The regions subjected to ratcheting and elastic shakedown predicted by the present model are superimposed [Colour figure can be viewed at wileyonlinelibrary.com]
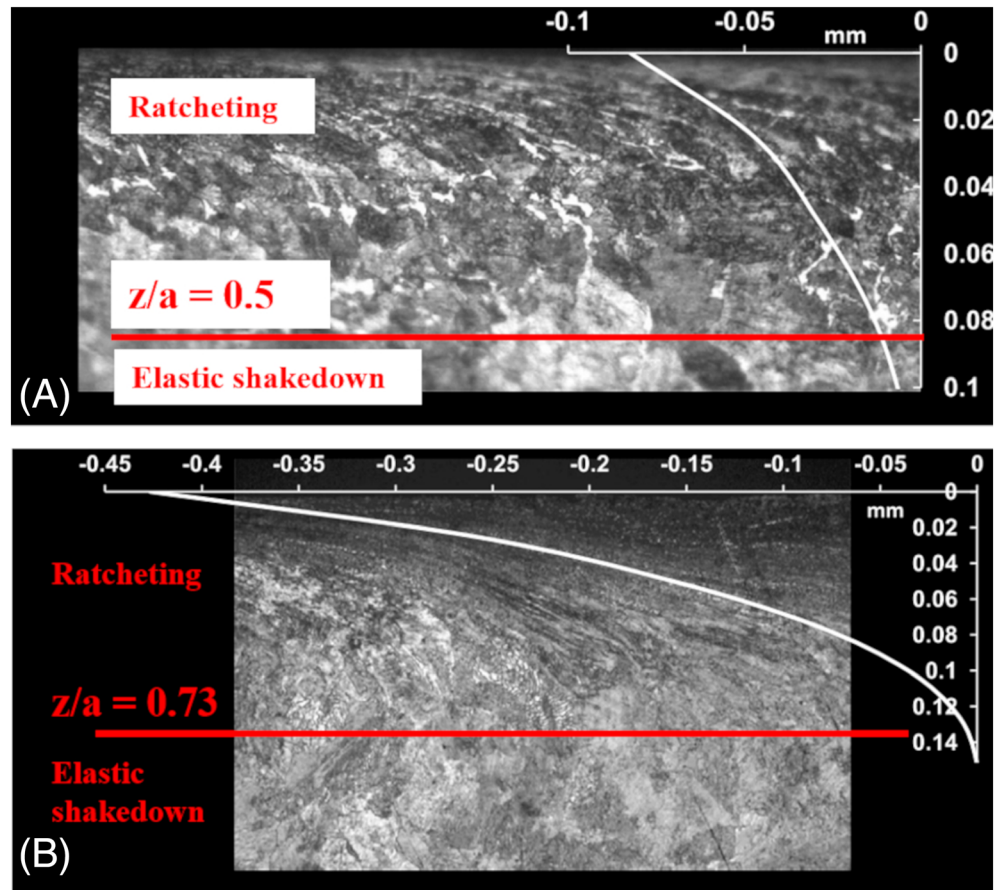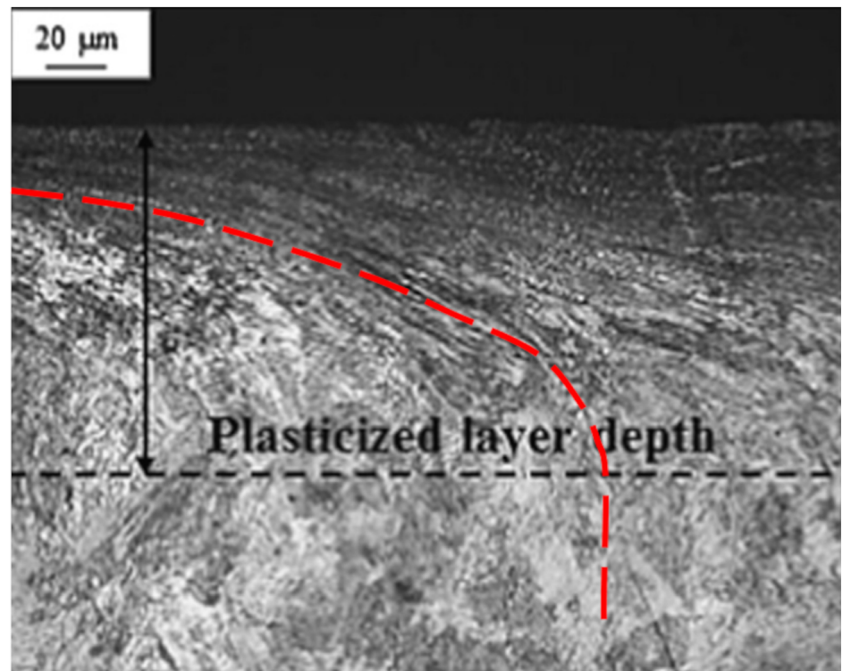

FIGURE 9 Deformed and undeformed regions in the wheel disk tested with $p_H = 777$ MPa[33] [Colour figure can be viewed at wileyonlinelibrary.com]

$$\sigma_{DV} = \max_t(\tau_a(t) + c\,\sigma_H(t)), \qquad (5.1)$$

where τ_a is the magnitude of the deviation of the shear stress from its midvalue during a stress cycle, $\sigma_H = (\sigma_x + \sigma_y + \sigma_z)/3$ is the hydrostatic stress, t is time, and c is a material parameter. The parameter c can be determined from the fatigue limits in alternating torsion τ_e and alternating bending σ_e as

$$c = 3\left(\frac{\tau_e}{\sigma_e} - \frac{1}{2}\right). \tag{5.2}$$

Fatigue initiation is predicted if $\sigma_{DV} > \tau_e$. The evaluation of the Dang Van stress was carried out using the algorithm proposed in Ekberg et al.[30] For the adopted steel, c is estimated as one third,[29] and the fatigue limit in alternating torsion is taken as 263 MPa.

Figure 10 shows how the Dang Van stress varies with depth. The horizontal blue solid line is the Dang Van threshold, above which crack initiation occurs. The decreasing trend under three-dimensional wheel–rail contact conditions is more pronounced than for the twin-disk conditions. This also indicates that twin-disk testing may yield more conservative results as compared with wheel–rail contacts.
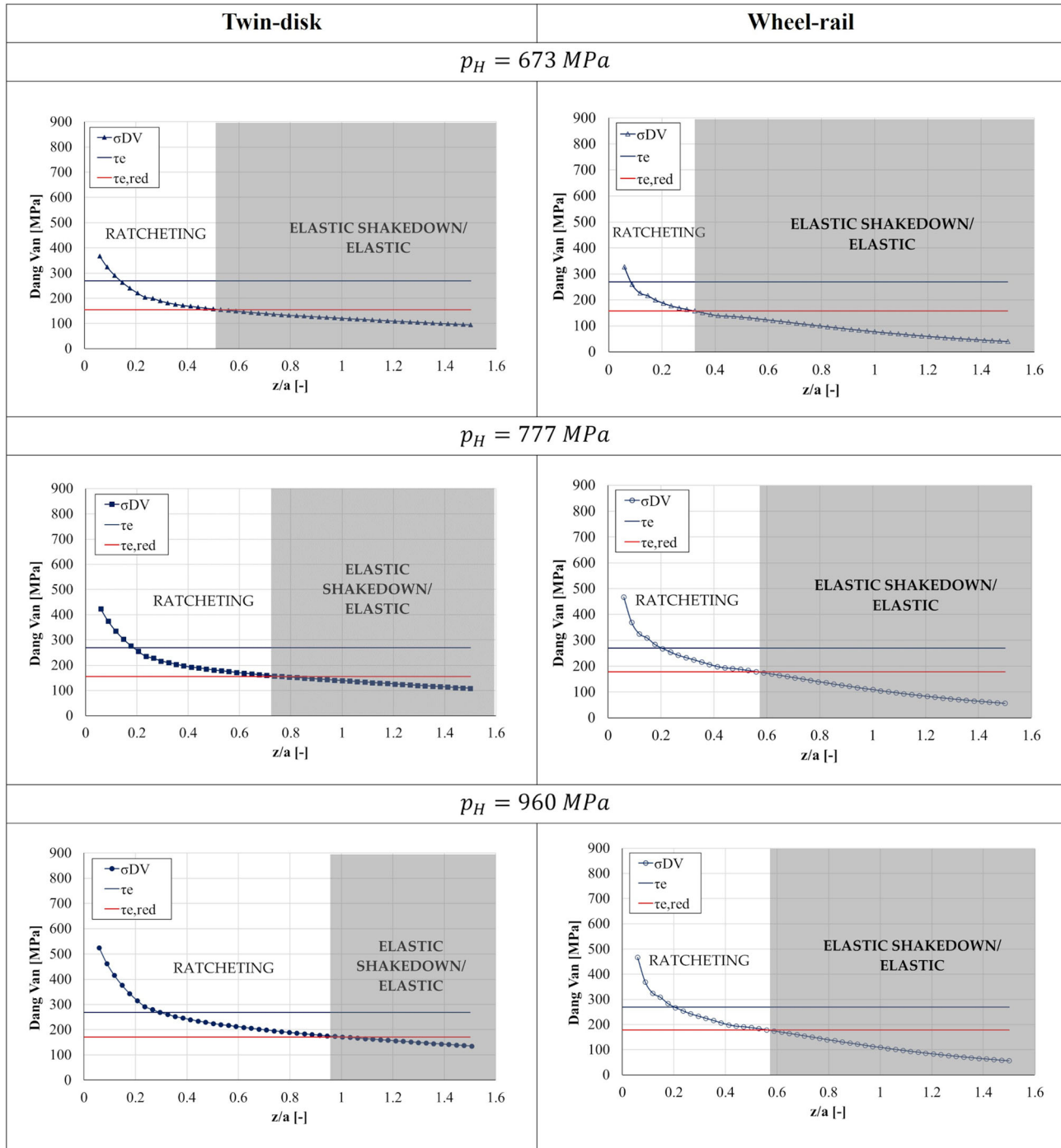

FIGURE 10 Dang Van equivalent stress as function of depth in twin-disk contact and in wheel–rail contact (σ_{DV}) for the investigated load cases. Dang Van thresholds τ_e and $\tau_{e,red}$ are indicated [Colour figure can be viewed at wileyonlinelibrary.com]

TABLE 7 Reduced torsional fatigue limits and maximum permissible defect sizes with respect to crack initiation

	Twin-disk			Wheel–rail		
Hertzian pressure (MPa)	672	777	963	672	777	963
$\tau_{e,red}$ (MPa)	154	155	170	163	174	179
$\sqrt{area}$ (μm)	472	454	260	335	226	191

The regions identified in gray in Figure 10 are those considered to be subjected to high cycle fatigue because they undergo either elastic shakedown or feature a fully elastic behavior. Notably, the stress magnitude in all these regions was below the Dang Van threshold, which would imply that no fatigue is initiated in these regions. However, the employed threshold does not consider the influence of material defects. This aspect should be considered because a large material volume is subjected to high stresses, and material defects therefore may exist. The reduced torsional fatigue limit $\tau_{e,red}$ owing to a material defect can be estimated by Murakami's equation[37]:

$$\tau_{e,red} = \frac{0.93}{F(b/a)} \frac{(HV + 120)}{(\sqrt{area})^{\frac{1}{6}}}, \qquad (5.3)$$

where HV is the Vickers hardness, $\sqrt{area}$ is the area of the precrack projected onto a plane perpendicular to the maximum tensile stress, a and t are the crack dimensions, and $F(t/a)$ is the function[37]

$$F(t/a) = 0.0957 + 2.11(t/a) - 2.26(t/a)^2 + 1.09(t/a)^3 - 0.196(t/a)^4. \qquad (5.4)$$

It must be pointed out that Murakami's equation can be applied to multiaxial conditions, although it was extrapolated from torsional tests because the crack mode propagation in the tests was mixed and analog to that in rolling contact.[37] The Vickers hardness of the steel was 242–268. Microscopic examination of the wheel disks revealed manganese sulfide inclusions. For our study, we used the maximum hardness, considering the $\sqrt{area}$ as the manganese sulfide inclusion length,[38] and we set $\tau_{e,red}$ as the maximum Dang Van stress calculated in the elastic (shakedown) areas. The resulting $\tau_{e,red}$ magnitudes are indicated in Figure 10 with a solid red line.

The maximum acceptable size $\sqrt{area}$ decreases with load and is smaller for the elliptical contact than for the line contact (see Table 7). This result might be unexpected because the line contact was earlier determined to be more conservative with respect to plastic deformations. However, the high magnitude elastic field in wheel–rail contact extends to deeper regions, and therefore, $\tau_{e,red}$ is lower. It should be pointed out that, for our purposes, we adopted $\tau_{e,red}$ as the maximum Dang Van admissible stress in the presence of inclusions in the elastic region, because this criterion is valid only whenever the material results in an elastic (shakedown) state. However, nothing can be inferred about surface cracking where the material plastically deforms, and consequently, the Dang Van criterion cannot be applied. Thus, this analysis focused on subsurface cracking, which is relatively rare but potentially more dangerous than surface cracking.[39]

The maximum defect size admissible for twin-disk contact was calculated to be approximately 260 μm, whereas that for the wheel–rail contact resulted in 191 μm. We can compare the former with the size found from an extreme value statistics of the disk material, where the maximum inclusion size expected was roughly 202 μm (this value was calculated on a circular crown with a depth equal to the semicontact Hertzian area[33]). Notably, the estimated maximum inclusion size for twin-disk contact was smaller than the admissible one, indicating no subsurface fatigue initiation from inclusions, as seen in the experimental tests, which also featured more cycles than the simulations. Regarding the full-scale elliptical contact condition, we refer to the EN13262 standard,[40] according to which the maximum macroinclusion acceptable in a railway wheel is 1 mm. It should be clarified that the macroinclusion this standard deals with refers to a depth of around 10–25 mm below the tread,[39,41] but subsurface fatigue can occur at a depth as shallow as 3–5 mm.[29,39] However, as a consequence of the reprofiling operation, the deeper regions reach the wheel's surface, and therefore, deeper regions end up closer to the surface. Given this, we can infer that the inclusion size calculated from Equation (5.3) still satisfies the standard requirements and is far below the threshold; on the other hand, we still cannot exclude the subsurface crack initiation will happen because we need the complete inclusion size distribution to estimate the most prominent inclusion using means of extreme value statistics.

6 | CONCLUSIONS

The nonlinear kinematic and isotropic hardening model of Chaboche–Lemaitre was applied to cyclic contact problems. Despite the lack of any relaxation procedure to evaluate residual stresses, the plastic strain magnitude as quantified by the shear component, which is the main

contributor to plastic deformation and RCF damage, is consistent with that calculated by FE simulations.

It is also worth stressing that the semianalytical model reduced the computational time by a factor of 30 to 150 times with respect to the FE analysis.

The proposed model was adopted to compare rolling contact problem in a full-scale rail–wheel elliptical contact with a small-scale twin-disk line contact. For the same maximum contact pressure, the plasticized layer is deeper under twin-disk contact conditions. All layers down to a depth of $z/a = 1.5$ deform plastically for at least one load cycle. In contrast, the deepest layers in the elliptical wheel–rail contact experienced an elastic response from the first cycle.

The Dang Van multiaxial fatigue criterion was applied to the subsurface layers subjected to high cycle fatigue. Considering a defect-free material, crack initiation was not expected because the equivalent stress is much lower than the fatigue threshold. Accounting for the influence of material defects, larger inclusions than those found in the investigated specimens were required to cause fatigue initiation. This was consistent with twin-disk experiments chosen as reference.

In conclusion, the proposed method offers complete damage evaluation and can consider multiple failure mechanisms such as shakedown, ratcheting, or high cycle fatigue by taking advantage of a fast calculation algorithm.

ACKNOWLEDGMENTS

CONFLICT OF INTERESTS
The authors declare that there is no conflict of interest that could be perceived as prejudicing the impartiality of the research reported.

AUTHOR CONTRIBUTIONS
Nicola Zani: writing – original draft, visualization, conceptualization, methodology, simulations Magnus Ekh: writing – review and editing, methodology Anders Ekberg: writing – review and editing, methodology Angelo Mazzù: writing – review and editing

DATA AVAILABILITY STATEMENT
Data are available upon request from the authors.

NOMENCLATURE

a	contact semiaxis (rolling direction)
$\sqrt{area}$	area of the precrack in Murakami's theory
b	isotropic saturation hardening parameter
c	material parameter in Dang Van criterion
C	kinematic hardening parameter
d	contact semiaxis (transverse direction)
f	friction coefficient
F	contact force
HV	Vickers hardness
L	transversal contact length in line contact
$p(x,y)$	Hertzian contact pressure distribution
p_H	maximum Hertzian contact pressure
$P(x,y)$	total surface traction force distribution
R	dragstress
R_∞	isotropic stress saturation
R_{1x}, R_{2x}	longitudinal radius of the contact bodies
R_{1y}, R_{2y}	transversal radius of the contact bodies
$\boldsymbol{X}$	backstress
γ	kinematic hardening parameter
$\dot{\boldsymbol{\varepsilon}}^{\boldsymbol{p}}$	plastic strain tensor evolution
λ	plastic multiplier
$\boldsymbol{\sigma_{dev}}$	deviatoric stress tensor
σ_{DV}	Dang Van stress
σ_e	fatigue limit in alternating bending
σ_H	hydrostatic stress
σ_y	initial yield stress
$\boldsymbol{\tau_a}$	magnitude of the deviation of the shear stress from its midvalue
τ_e	fatigue limit in alternating torsion
$\tau_{e,red}$	reduced fatigue limit in alternating torsion
Φ	yield function

ORCID
Nicola Zani https://orcid.org/0000-0001-6808-8852
Magnus Ekh https://orcid.org/0000-0001-6925-7806
Anders Ekberg https://orcid.org/0000-0002-3219-1855
Angelo Mazzù https://orcid.org/0000-0002-6074-3143

REFERENCES
1. Braghin F, Bruni S, Resta F. Wear of railway wheel profiles: a comparison between experimental results and a mathematical model. *Veh Syst Dyn*. 2003;37(sup1):478-489.
2. Bruni S, Collina A, Diana G, Vanolo P. Lateral dynamics of a railway vehicle in tangent track and curve: tests and simulation. *Veh Syst Dyn*. 2000;33(sup1):464-477.
3. Faccoli M, Petrogalli C, Lancini M, Ghidini A, Mazzù A. Effect of desert sand on wear and rolling contact fatigue behaviour of various railway wheel steels. *Wear*. 2018; 396–397:146-161.

4. Grieve DG, Dwyer-Joyce RS, Beynon JH. Abrasive wear of railway track by solid contaminants. *Proc Inst Mech Eng Part F J Rail Rapid Transit*. 2001;215(3):193-205.

5. Lewis R, Dwyer-Joyce RS. Wear at the wheel/rail interface when sanding is used to increase adhesion. *Proc Inst Mech Eng Part F J Rail Rapid Transit*. 2007;220(1):29-41.

6. Meierhofer A, Trummer G, Bernsteiner C, Six K. How the weather in autumn influenced the wheel-rail traction characteristic during vehicle tests. In: *Proceedings of the 11th International Conference on Contact Mechanics and Wear of Rail/Wheel Systems (CM2018)*. Delft, The Netherlands; 2018: 727-733.

7. Chen H, Furuya T, Fukagai S, Saga S, Murakami K, Ban T. Survey occurrence of wheel slipping/sliding caused by fallen leaves on the test line. In: *Proceedings of the 11th International Conference on Contact Mechanics and Wear of Rail/Wheel Systems (CM2018)*. Vol. 1; 2018:140-146.

8. Makino T, Kato T, Hirakawa K. The effect of slip ratio on the rolling contact fatigue property of railway wheel steel. *Int J Fatigue*. 2012;36(1):68-79.

9. Mazzù A, Provezza L, Zani N, Petrogalli C, Ghidini A, Faccoli M. Effect of shoe braking on wear and fatigue damage of various railway wheel steels for high speed applications. *Wear*. 2019;434–435:203005.

10. Mazzù A, Petrogalli C, Lancini M, Ghidini A, Faccoli M. Effect of wear on surface crack propagation in rail–wheel wet contact. *J Mater Eng Perform*. 2018;27(2):630-639.

11. Al-Juboori A, Zhu H, Wexler D, et al. Evolution of rail surface degradation in the tunnel: the role of water on squat growth under service conditions. *Eng Fract Mech*. 2019;209:32-47.

12. Zani N, Chaise T, Ghidini A, Faccoli M, Mazzù A. Numerical study about the effect of bainitic traces on plasticity in ferritic-pearlitic railway wheels. *Proc Institutions Mech Eng Part F J Rail Rapid Transit*. 2021;235(6):726-740.

13. Mazzù A, Ghidini A, Zani N, Faccoli M. A simplified numerical study of wheel/rail material coupling in presence of solid contaminants. *Tribol. - Mater. Surf. Interfaces*. 2021;15(2): 102-114.

14. Gallego L, Nélias D, Deyber S. A fast and efficient contact algorithm for fretting problems applied to fretting modes I, II and III. *Wear*. 2010;268(1):208-222.

15. Amuzuga KV, Chaise T, Duval A, Nelias D. Fully coupled resolution of heterogeneous elastic–plastic contact problem. *J Tribol*. 2016;138(2):1-22.

16. Mazzù A, Ghidini A, Zani N, Faccoli M. Study of wheel/rail material coupling in presence of solid contaminants. In: *Proceedings of the 11th International Conference on Contact Mechanics and Wear of Rail/Wheel Systems (CM2018)*. Delft, The Netherlands; 2018:701-710.

17. Ghidini A, Diener M, Mazzù A, Zani N, Petrogalli C, Faccoli M. Considerations about microstructure of solid wheels with traces of bainite. *Ingegneria Ferroviaria*. 2020;3: 165-178.

18. Foletti S, Desimone HJ. A semi-analytical approach for two-dimensional rolling/sliding contact with applications to shakedown analysis. *Wear*. 2007;262(7–8):850-857.

19. Mazzù A, Battini D. A model for the assessment of wheel–rail contact in the presence of solid contaminants. *Tribol Trans*. 2019;62(2):230-238.

20. Mazzù A, Donzella G. A model for predicting plastic strain and surface cracks at steady-state wear and ratcheting regime. *Wear*. 2018;400–401:127-136.

21. Jiang Y, Sehitoglu H. An analytical approach to elastic-plastic stress analysis of rolling contact. *J Tribol*. 1994;116(3):577-587.

22. Qi Z, Li B, Xiong L. An improved algorithm for McDowell's analytical model of residual stress. *Front Mech Eng*. 2014;9(2): 150-155.

23. Merwin JE, Johnson KL. An analysis of plastic deformation in rolling contact. *P I Mech Eng*. 1963;117(1):676-690.

24. Bhargava V, Hahn GT, Rubin CA. An elatic-plastic finite element model of rolling contact. Part 1: analysis of single contacts. *J Appl Mech*. 1985;52(1):67-74.

25. Chaboche JL. Constitutive equations for cyclic plasticity and cyclic viscoplasticity. *Int J Plast*. 1989;5(3):247-302.

26. Armstrong PJ, Frederick CO. A mathematical representation of the multiaxial Bauschinger effect. *Mater High Temp*. 1966;24(1):1-26.

27. Voce E. The relationship between stress and strain for homogeneous deformation. *J Inst Met*. 1948;74:537-562.

28. Donzella G, Mazzù A, Petrogalli C. Competition between wear and rolling contact fatigue at the wheel–rail interface: some experimental evidence on rail steel. *Proc Inst Mech Eng Part F J Rail Rapid Transit*. 2009;223(1):31-44.

29. Desimone H, Bernasconi A, Beretta S. On the application of Dang Van criterion to rolling contact fatigue. *Wear*. 2006; 260(4–5):567-572.

30. Ekberg A, Kabo E, Andersson H. An engineering model for prediction of rolling contact fatigue of railway wheels. *Fatigue Fract Eng Mater Struct*. 2002;25(10):899-909.

31. Bernasconi A, Filippini M, Foletti S, Vaudo D. Multiaxial fatigue of a railway wheel steel under non-proportional loading. *Int J Fatigue*. 2006;28(5–6):663-672.

32. Van KD, Griveau B, Message O. On a new multiaxial fatigue limit criterion theory and application, biaxial and multiaxial fatigue. *Mater Sci*. 1982;479-496.

33. Mazzù A, Petrogalli C, Faccoli M. An integrated model for competitive damage mechanisms assessment in railway wheel steels. *Wear*. 2015;322–323:181-191.

34. Donzella G, Faccoli M, Mazzù A, Petrogalli C, Roberti R. Progressive damage assessment in the near-surface layer of railway wheel–rail couple under cyclic contact. *Wear*. 2011;271(1–2):408-416.

35. Abaqus. *Abaqus Analysis User's Manual*. Providence, Rhode Island: Simulia; 2020.

36. Ekberg A. Rolling contact fatigue of railway wheels—a parametric study. *Wear*. 1997 Nov;211(2):280-288.

37. Murakami Y, Takahashi K. Torsional fatigue of a medium carbon steel containing an initial small surface crack introduced by tension-compression fatigue: crack branching, non-propagation and fatigue limit. *Fatigue Fract Eng Mater Struct*. 1998;21(12):1473-1484.

38. ASTM E 2283-03. Standard practice for extreme value analysis of nonmetallic inclusion in steel and other microstructural features. In: *Book of Standards*; 2003.

39. Ekberg A, Åkesson B, Kabo E. Wheel/rail rolling contact fatigue—probe, predict, prevent. *Wear*. 2014;314(1–2):2-12.

40. EN 13262+A1. Railway applications—wheelsets and bogies—axles—product requirements. 2010. 1–61.

41. Beretta S, Donzella G, Roberti R, Ghidini A. Contact fatigue propagation of deep defects in railway wheels. In: *Proceedings*

of the 13th European Conference on Fracture—ECF13. San Sebastian; 2000:147-154.

42. Johnson KL. *Contact Mechanics.* UK: Cambridge University Press; 1985.

APPENDIX A.

McEWEN'S EQUATIONS FOR LINE CONTACT PROBLEMS[42]

If two cylinders in contact are considered, the stresses acting on the xz plane can be found by McEwen's equations (Figure A1):

$$\sigma_{x,p} = -\frac{p_H}{a}\left[m\left(1+\frac{n^2+z^2}{m^2+n^2}\right)-2z\right], \quad (A1)$$

$$\sigma_{z,p} = -\frac{p_H}{a}m\left(1+\frac{n^2+z^2}{m^2+n^2}\right), \quad (A2)$$

$$\tau_{xz,p} = -\frac{P_H}{a}n\left(\frac{m^2-z^2}{m^2+n^2}\right), \quad (A3)$$

$$\sigma_{x,q} = -\frac{\mu P_H}{a}\left\{n\left(2-\frac{z^2-m^2}{m^2+n^2}\right)-2x\right\}, \quad (A4)$$

$$\sigma_{z,q} = -\mu\,\tau_{xz,p}, \quad (A5)$$
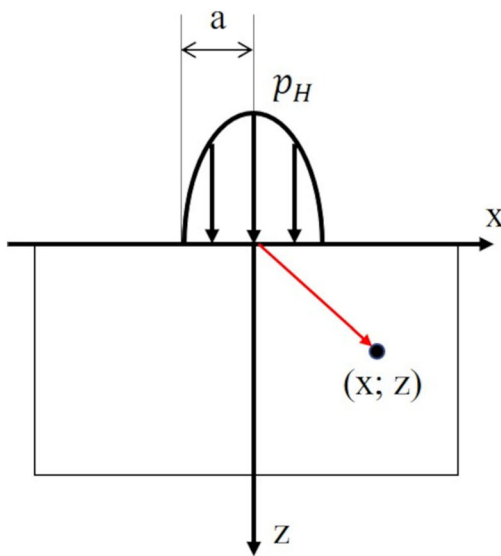
$$\tau_{xz,q} = -\mu\sigma_{z,p}, \quad (A6)$$
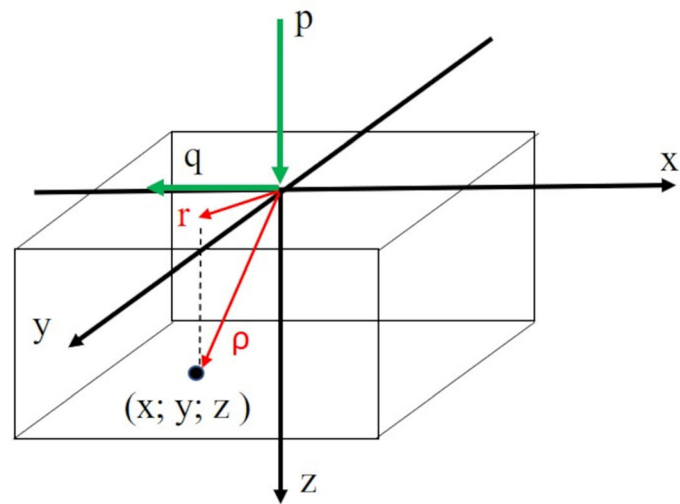
$$\sigma_y = -\nu(\sigma_x+\sigma_z), \quad (A7)$$

where

$$m^2 = 0.5\left\{\left[\left(a^2-x^2+z^2\right)^2+4x^2z^2\right]^2+\left(a^2-x^2+z^2\right)\right\}, \quad (A8)$$

$$n^2 = 0.5\left\{\left[\left(a^2-x^2+z^2\right)^2+4x^2z^2\right]^2-\left(a^2-x^2+z^2\right)\right\}. \quad (A9)$$

The signs of m and n are the same as z and x, respectively. The total stress of each component is obtained by adding the tangential contribution to the normal one.

FIGURE A1 Geometry and parameters in line contact and general contact [Colour figure can be viewed at wileyonlinelibrary.com]

APPENDIX B.

BOUSSINESQ'S EQUATIONS FOR GENERAL CONTACT PROBLEMS[42]

The following equations are the solution of the Boussinesq potential functions to solve a general distributed normal and tangential load. We indicate with the subscripts p and q the stress components referring to the normal and tangential load, respectively (Figure A1).

$$\sigma_{x,p} = \frac{p}{2\pi}\left[\frac{(1-2\nu)}{r^2}\left\{\left(1-\frac{z}{\rho}\right)\frac{x^2-y^2}{r^2}+\frac{zy^2}{\rho^3}\right\}-\frac{3zx^2}{\rho^5}\right], \tag{B1}$$

$$\sigma_{y,p} = \frac{p}{2\pi}\left[\frac{(1-2\nu)}{r^2}\left\{\left(1-\frac{z}{\rho}\right)\frac{y^2-x^2}{r^2}+\frac{zx^2}{\rho^3}\right\}-\frac{3zy^2}{\rho^5}\right], \tag{B2}$$

$$\sigma_{z,p} = -\frac{3p}{2\pi}\frac{z^3}{\rho^5}, \tag{B3}$$

$$\tau_{xy,p} = \frac{p}{2\pi}\left[\frac{(1-2\nu)}{r^2}\left\{\left(1-\frac{z}{\rho}\right)\frac{xy}{r^2}+\frac{xyz}{\rho^3}\right\}-\frac{3xyz}{\rho^5}\right], \tag{B4}$$

$$\tau_{xz,p} = -\frac{3p}{2\pi}\frac{xz^2}{\rho^5}, \tag{B5}$$

$$\tau_{yz,p} = -\frac{3p}{2\pi}\frac{yz^2}{\rho^5}, \tag{B6}$$

$$\frac{2\pi\sigma_{x,q}}{q_x} = -\frac{3x^3}{\rho^5}+(1-2\nu)\left\{\frac{x}{\rho^3}-\frac{3x}{\rho(\rho+z)^2}+\frac{x^3}{\rho^3(\rho+z)^2}+\frac{2x^3}{\rho^2(\rho+z)^3}\right\}, \tag{B7}$$

$$\frac{2\pi\sigma_{y,q}}{q_x} = -\frac{3xy^2}{\rho^5}+(1-2\nu)\left\{\frac{x}{\rho^3}-\frac{x}{\rho(\rho+z)^2}+\frac{xy^2}{\rho^3(\rho+z)^2}+\frac{2xy^2}{\rho^2(\rho+z)^3}\right\}, \tag{B8}$$

$$\frac{2\pi\sigma_{z,q}}{q_x} = -\frac{3xz^2}{\rho^5}, \tag{B9}$$

$$\frac{2\pi\tau_{xy,q}}{q_x} = -\frac{3xy^2}{\rho^5}+(1-2\nu)\left\{-\frac{y}{\rho(\rho+z)^2}+\frac{x^2y}{\rho^3(\rho+z)^2}+\frac{2x^2y}{\rho^2(\rho+z)^3}\right\}, \tag{B10}$$

$$\frac{2\pi\tau_{yz,q}}{q_x} = -\frac{3xyz}{\rho^5}, \tag{B11}$$

$$\frac{2\pi\tau_{xz,q}}{q_x} = -\frac{3x^2z}{\rho^5}, \tag{B12}$$

with ρ and r defined as follows:

$$\rho^2 = x^2+y^2+z^2, \tag{B13}$$

$$r^2 = x^2+y^2. \tag{B14}$$